Fuel Debris Simulants for The Gripper Design of Decommissioning Robot Manipulator in Fukushima Daiichi (1F)

Shinsuke Nakashima[1], Alessandro Moro[2], Ren Komatsu[1], Angela Faragasso[1], Nobuto Matsuhira[1], Hanwool Woo[3], Kuniaki Kawabata[4], Atsushi Yamashita[5], Hajime Asama[1]

***Abstract*— Fuel debris retrieval is the fundamental task for decommissioning Fukushima Daiichi (1F). The presence of high radiation intensively affects the performance of conventional robotic systems which in many cases, due to failure of the electronic components, become obstacles to be retrieved. New systems and techniques are required to cope with the current limitations and find efficient solutions. This research presents the design approach exploiting rapid prototyping of a gripper system for a manipulator used to retrieve fuel debris on the bottom of the PCV (Primary Container Vessel). Modeling of the gripper is performed in simulations to find the relations between the ligaments that constrain the bending motion. The debris simulants and the fabricated 3D-printed gripper are shown.**

I. Introduction

Fuel debris retrieval is one of the significant steps for decommissioning Fukushima-Daiichi (1F). Due to the high-dose environment in the power plant structure, the monitoring and operation are severe for the human operators. In the PCV (PCV: Primary Containment Vessel), especially, it is required to introduce robotic teleoperation for the decommissioning process. In recent years, rigorous investigations have been unveiling the rough distribution of the fuel debris near the entrance of PCV [1]. However, fuel debris retrieval from the bottom of the PCV is still one of the most challenging tasks (Fig. 1). This research describes the design approach of a robot gripper to be embedded in a long-reach arm for fuel debris retrieval. The manipulator goes through the access route to the area above the debris, and the gripper's debris retrieval task has to overcome challenges such as gamma-ray radiation, shock resistance, and underwater operation. In this study, we tackle the problems by exploiting rapid prototyping for developing the debris simulants and the gripper. Because the power plant's situation is unclear and unstable, the appropriate gripper configuration should be easily modified. Facilitating grasp verification through the sample payload and easy-to-repair hardware accelerates the design iteration of the gripper hardware. First, we will describe the debris' characteristics as a payload. Next, we mention the fabrication process of the debris simulants to facilitate manipulation testing. Preliminary experiments of the gripper are also reported from which the conclusions are drawn.

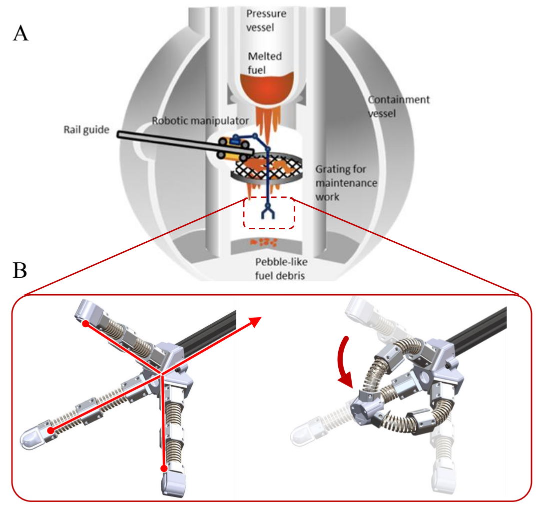

Fig. 1. Fuel debris retrieval task. A) A robotic manipulator enters the PCV through a rail guide. The robot arm extends the structure of 4 [m] to approach and grasp the target: Pebble-like fuel debris. B) Robot gripper at the tip of the robot arm. The gripper is characterized by adaptivity, robustness, underwater performance, and radiation tolerance. Target weight of the debris is from 50 [g] to 500 [g].

II. Related works

Object datasets have been the driving force to improve the manipulation research. For example, Yale-CMU-Berkeley dataset [2] consists of 600 RGB-D images and the 3D models of real-world objects in the human environment such as houses and factories. The dataset is often used for the benchmark of robotic manipulation[3]. Exploiting datasets accelerates the trials in the simulation and the real world. In those days, photorealistic simulations and massive computational resources aided the transfer of knowledge from simulation to the real world. The datasets also aid the processes of the gripper design validation [4]. These activities mainly focused on the manipulation of household rigid objects.

[1]The authors are with Department of Precision Engineering, The University of Tokyo, 7-3-1 Hongo, Bunkyo-ku, Tokyo 113-8656, JAPAN nakashima, komatsu, faragasso, matsuhira, yamashita, asama at robot.t.u-tokyo.ac.jp

[2]The author is with RITECS Inc., 3-5-11 Shibasaki-cho, Tachikawa-shi, Tokyo 190-0023, JAPAN moro at robot.t.u-tokyo.ac.jp

[3]The author is with Department of Mechanical Systems Engineering, Kogakuin University, 2665-1 Nakano-cho, Hachioji-shi, Tokyo 192-0015, JAPAN at13710 at g.kogakuin.jp

[4]The author is with Radiation Sensing and Digitization Group, Collaborative Laboratories for Advanced Decommissioning Science (CLADS), Fukushima Research & Engineering Institute, Japan Atomic Energy Agency (JAEA), 1-22, Nakamaru, Yamadaoka, Narahamachi, Futaba, Fukushima, 979-0513, JAPAN yamashita at robot.t.u-tokyo.ac.jp

[5]The author is with Department of Human and Engineered Environmental Studies,Graduate School of Frontier Sciences, The University of Tokyo, 5-1-5 Kashiwanoha, Kashiwa, Chiba 2778563, JAPAN yamashita at robot.t.u-tokyo.ac.jp

Additionally, robots' soft manipulation is also in rigorous development. For example, food samples are used for evaluating the robot's capability of food manipulation [5]. In recent years, a raspberry physical twin contributed to the robot's acquisition of the picking strategy not to break the real raspberries in the field [6].

Similarly, fuel debris simulants help develop and deploy the robot manipulators to retrieve the real fuel debris. However, due to the unknown characteristics of the fuel debris, the studies dealing with the payload features of the fuel debris are still limited. For example, fuel debris has been featured in the chemical context. Research is ongoing to understand the phenomena and the resultant composition of the fuel debris [7]. However, fuel debris has been a niche object for robot manipulation.

III. Fuel Debris Simulants

This section presents the characteristics of the fuel debris focusing on the features as a payload. In addition, it shows the method to prepare the debris simulant used to conduct grasping tests.

A. The Characteristics of Fuel Debris as Payload

This section describes the fuel debris to be grasped and to be retrieved. Fuel debris (usually referred to as "debris") is fuel in the solid state that is generated by the melting down process inside the PCV structure. The fuel debris has different properties such as density, elastic modulus, fracture toughness, etc., depending on the material of the melted structure [8], [9]. Currently, the PCV is being cooled down by continuous injection of cooling water, and the debris is immersed in shallow water at the bottom of the PCV. The debris is roughly characterized by the following properties.

1) Pebble
2) Semisolid
3) Plate

are the typical categories of fuel debris [10]. Pebble-like debris is a solid object. They are composed of stable matters. Metallic debris is heavy and tough, and ceramic-based debris is fragile and relatively light. Semisolid debris includes reactive elements that might radically react to water vapor. Plate-like debris adheres to the PCV structure firmly, which makes it harder to remove from the PCV. This research aims at the retrieval of pebble-like debris. Because common debris materials include solid oxide and heavy metal, we select cementitious and metallic materials for manufacturing the debris simulant. The payload weight is from 50 $[\mathrm{g}]$ to 500 $[\mathrm{g}]$.

TABLE I
Properties of the debris simulant

Material	PLA	Cement	Metallic (LMPA)
Weight $[\mathrm{g}]$	25	54	200
Density $[\mathrm{g/cm^3}]$	1.3	3.0	8.0
Process time [min]	60	30	30
Method	3D print	Casting	Casting

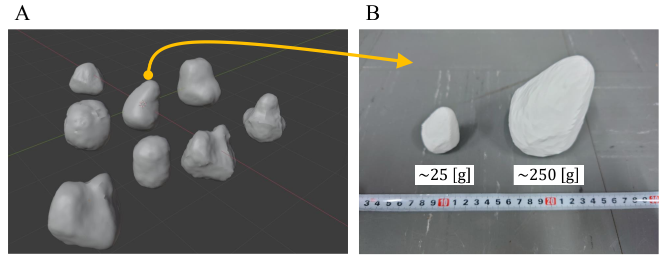

Fig. 2. Debris simulants. A) Output of Blender Rock Generator [11]. The software generates random rock shapes with different properties. B) 3D printed resin model made from tough PLA filament. Scaling of the .stl file alters the size of the output product flexibly.

B. Manufacturing Process of The Debris Simulants

In the future development process of grippers and robotic arms, a simulated environment and simulated debris are necessary for conducting tests in a real environment. This section describes the fabrication process of simulated debris. In the previous studies, the construction of simulated debris has been done to predict and understand the properties of fuel debris, and the composition of the products has been analyzed by simulating the composition and reaction of the PCV structure and fuel [12], [13]. Here, we performed detailed studies on the material properties of the debris to characterize the properties of the objects that have to be grasped and recovered by the robot. Specifically, the model was designed to reproduce the size scale, density, compressive strength, etc., to be used in the approach and grasping simulations. Firstly, we aimed to utilize the same geometry in the actual machine and the simulation model. The procedure is shown in Fig. 2. The geometry is generated by "Rock Generator", an add-on for the 3D modeling software "Blender"[14]. It is possible to generate rock models in batch format with desired dimensions and properties. The geometry file can be imported into a simulator or a resin model can be output by using a 3D printer. In addition, by molding the resin model,

Fig. 3. Silicone casting of debris simulants using LMPA (Low melting point alloy). A) Pouring molten metal into the silicone mold. We used a soldering iron to melt the LMPA ingot. B) Solidification of liquid metal in the silicone mold. The process takes tens of minutes. C) Output of the cement and metallic debris simulants. the simulants capture the shape of the resin model.

it will be possible to fabricate simulated debris with various densities and strength properties, replicated with cement and low-melting-point metals (Fig. 3). Table I describes the properties of the debris simulant. Note that the casting process of cement and LMPA requires the resin sample and the silicone mold. Making a resin sample and silicone mold requires less than one hour for each sample.

IV. Gripper Design Approach

A. Gripper's Joint Structure

Various grasping mechanisms have been proposed, such as a vacuum gripper, and a multi-fingered hand with rigid links.

In this study, we introduce a configuration with a multi-fingered gripper without axial joints for structural robustness, adaptability to the grasped object, and prevention of structural destruction and release of the grasped object due to collisions. Based on relevant works [15], [16], we generated bending motion by utilizing helical spring joints and fiber constraints. Because the spring structure is common, spring parameter selection enables the developers to deal with divergent grasp objects. Altering the wrist component is effective for the development of different finger numbers.

A motor-driven tendon of polymeric wire "Dyneema" is mounted inside the finger structure and is wound by a brushless motor away from the gripper body. The tendon-driven system makes it possible to separate the drive source from the object to be driven [17], [18]. The bottom of the pedestal where debris exists is an environment where gamma rays and shallow water exist, and separating the minimum electrical components for driving from the main body of the gripper contributes to improving the waterproof and radiation resistance of this robot gripper. The "Moteus open-source brushless DC controller" was used as the drive system for the brushless motor.

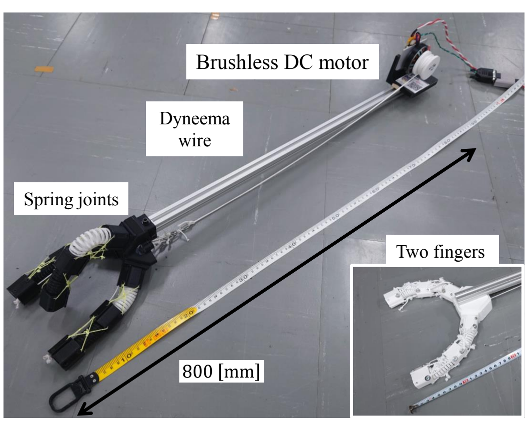

Fig. 4. Gripper overview. Overall size is 800 [mm]. The gripper's fingers are equipped with spring joints. The brushless DC motor pulls the tendon wire, which generates the bending motion of the fingers. Because the grippers have common hardware, subtle change to the wrist part makes additional variations of the gripper such as the two-fingered model.

B. Gripper's Ligamentous Constraints

The subsection explains the wire constraints or ligaments of a spring joint. Because the spring deforms in any direction, selecting the proper ligaments' attachments is necessary to generate the desired motion. The study investigates the length change of the ligament wire depending on the spring's bending and twisting motion.

The deformation of the spring can be described using the constant-curvature model [19] shown in Eq. (1) and Fig. 5. We utilize the homogeneous transformation matrix to calculate the fixture points of the ligaments. Then, the calculation of the ligaments' length values becomes possible.

$$\begin{aligned}\mathbf{r}(\theta) &= \begin{bmatrix} x(\theta) \\ y(\theta) \end{bmatrix} \\ &= L \begin{bmatrix} \frac{1-\cos\theta}{\theta} \\ \frac{\sin\theta}{\theta} \end{bmatrix}\end{aligned} \tag{1}$$

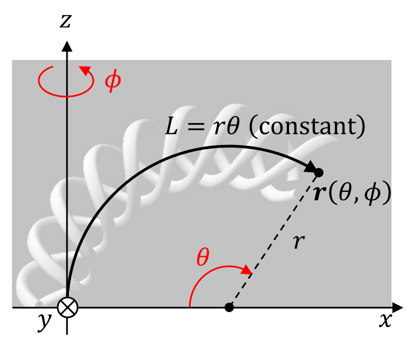

Fig. 5. Constant curvature model.

Fig. 6 depicts the parametric curve predicted by the constant curvature model. The total length L of the spring is assumed to be constant.

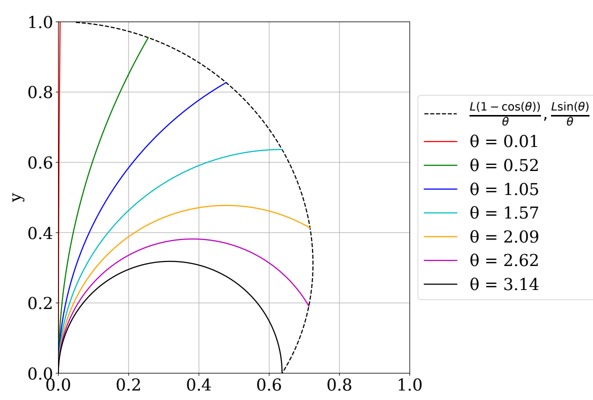

Fig. 6. Parametric curve with different θ [rad]. The colored solid lines show the spine curve of the spring's central axis. The black dotted line shows the envelope. The envelope is the trajectory of the tip position of the spring.

We now consider the change in the length of the ligament when the spring is subjected to the desired bending deformation while the restraining wire is in contact with the spring (Fig. 7). It is assumed that the strings restrain the ligaments and cannot be lengthened beyond the length at which they are attached. On the other hand, the shortening deformation corresponds to the slack of the ligament. In the ligament, there are parallel ligaments and cross ligaments, each of which acts as a resistance to the translational and the rotational motions. Note that the initial length of the cross ligament is larger than that of the parallel ligament. In addition, because the ligament attachment is performed while the spring is stretched, the ligament cannot be elongated from the length by the spring's bending motion.

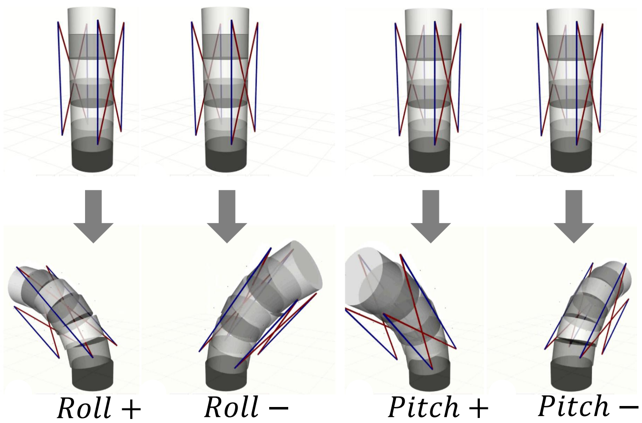

Fig. 7. Spring with the ligamentous constraints. The red multilink shows a spring. Yellow lines indicate the wire ligaments that constrain the spring's deformation.

Figure 8 illustrates the notation of the fixture points. The fixture points are eight. The spring is assumed to have eight ligaments.

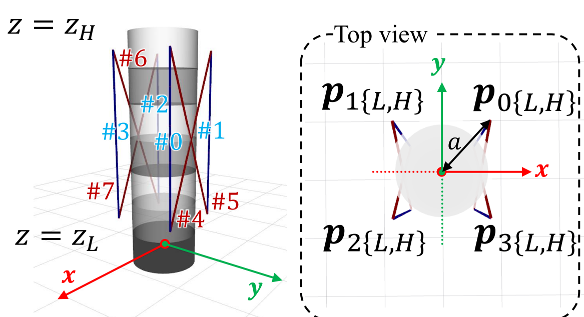

Fig. 8. Ligament notations.

Equation (2) depicts the homogeneous transformation matrix at the tip of the spring.

$$\mathbf{T}(\theta,\phi) = \begin{bmatrix} \mathbf{R}(\theta,\phi) & \mathbf{r}(\theta,\phi) \\ \mathbf{0}^{\mathrm{T}} & 1 \end{bmatrix} \tag{2}$$

$$\mathbf{R}(\theta,\phi) = \begin{bmatrix} \cos\phi\cos\theta & -\sin\phi & \cos\phi\sin\theta \\ \sin\phi\cos\theta & -\cos\phi & \sin\phi\sin\theta \\ -\sin\theta & 0 & \cos\theta \end{bmatrix} \tag{3}$$

$$\mathbf{r}(\theta,\phi) = \begin{bmatrix} \dfrac{L\cos\phi(1-\cos\theta)}{\theta} \\ \dfrac{L\sin\phi(1-\cos\theta)}{\theta} \\ \dfrac{L\sin\theta}{\theta} \end{bmatrix} \tag{4}$$

The fixture points of the ligaments are defined by Eqs. (5), (6) and (7). There are four fixture points for each height. The spring design affects the points' numbers and locations.

$$i \in \{0,1,2,3\} \tag{5}$$

$$j \in \{L,H\} \tag{6}$$

$$\mathbf{p}_{ij} = \begin{bmatrix} a(\cos\frac{\pi}{2}i+\frac{\pi}{4}) \\ a(\sin\frac{\pi}{2}i+\frac{\pi}{4}) \\ z_j \end{bmatrix} \tag{7}$$

From Eqs. (2) and (7), we can derive Eq. (8) by assuming that $z_L = 0$ and $z_H = L$.

$$\mathbf{p}_{i_H} = \mathbf{T}(\theta,\phi)\mathbf{p}_{i_L} \tag{8}$$

Table II explains the notation of the ligaments. It should be noted that the ligaments from #0 to #3 are parallel. On the other hand, the items from #4 to #7 are cross ligaments.

TABLE II
NOTATION OF THE LIGAMENTS

Number	Connection
#0	$\mathbf{p}_{0_L} \rightarrow \mathbf{p}_{0_H}$
#1	$\mathbf{p}_{1_L} \rightarrow \mathbf{p}_{1_H}$
#2	$\mathbf{p}_{2_L} \rightarrow \mathbf{p}_{2_H}$
#3	$\mathbf{p}_{3_L} \rightarrow \mathbf{p}_{3_H}$
#4	$\mathbf{p}_{0_L} \rightarrow \mathbf{p}_{1_H}$
#5	$\mathbf{p}_{1_L} \rightarrow \mathbf{p}_{0_H}$
#6	$\mathbf{p}_{2_L} \rightarrow \mathbf{p}_{3_H}$
#7	$\mathbf{p}_{3_L} \rightarrow \mathbf{p}_{2_H}$

By calculating the vector norm, we can estimate the displacement of each ligament. For example, the length of the ligament #0 can be calculated as $\|\mathbf{p}_{0_H} - \mathbf{p}_{0_L}\|$. For calculation, the parameters are set as follows.

$$L = 20\,[\mathrm{mm}] \tag{9}$$

$$a = 5\,[\mathrm{mm}] \tag{10}$$

First, we investigate the change in ligament length when bending around the roll axis is applied to a spring (Fig. 9). The cross ligament is longer than the parallel ligament at roll angle = 0 [rad]. The ligament length change when roll angle displacement is applied is similar for both the cross ligaments and the parallel ligaments, indicating that both ligament restraints contribute similarly.

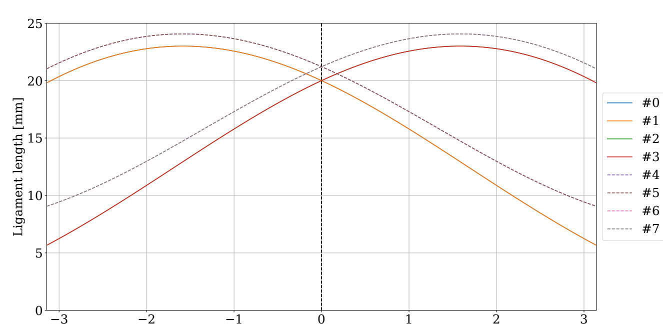

Fig. 9. Ligament length for roll rotation.

Next, we consider the change in ligament length when bending around the pitch axis is applied to the spring (Fig. 10). Note that the cross ligament is longer than the parallel ligament at Pitch angle = 0 [rad]. The ligament length change with pitch angle displacement is small for the cross ligament and large for the parallel ligament. In particular, the length of the cross ligament is the largest at Pitch angle=0 in all cases, suggesting that the cross ligament is a ligament that constrains the spring while allowing its motion around the pitch axis. To achieve the rotation $\theta_p > 0$, #1 and #2 should be removed. On the other hand, #0 and #3 do not have to be removed.

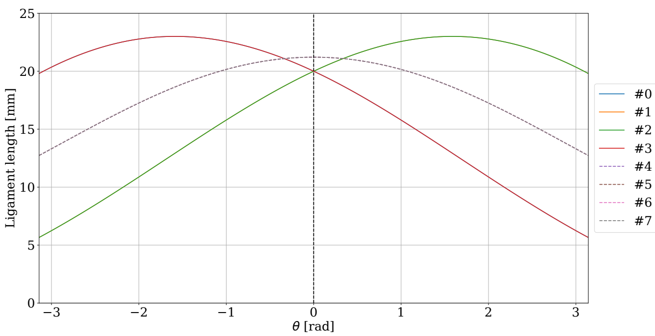

Fig. 10. Ligament length for pitch rotation.

Finally, we calculate the change in ligament length when bending around the yaw axis is applied to the spring (Fig. 11). Note that the cross ligament is longer than the parallel ligament at Yaw angle = 0 [rad]. The ligament length change with Yaw angular displacement is larger for the cross ligament and smaller for the parallel ligament. In particular, the parallel ligament has the smallest length at Pitch angle=0 in all cases, suggesting that the parallel ligament is a ligament that strongly constrains the motion of the spring around the yaw axis.

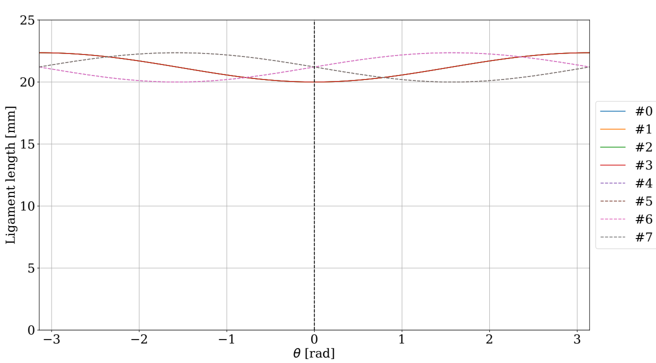

Fig. 11. Ligament length for yaw rotation.

The summary is shown in Table III. A ligament can perform the rotation if every ligament shows a minus. Otherwise, the rotation is constrained by the ligaments. Regarding pitch motion, ligaments #1 and #2 show plus. That is, they have to be removed. The rest ligaments block other motions. Therefore, we removed the ligaments #1 and #2 from the designed gripper.

As a limitation, the calculation assumes the straight ligament. That is, the collision between the ligaments and the spring itself is not calculated. As shown in Fig. 7, the large deflection makes the penetration by the ligament, which does not occur in the real world. Calculation of the geodesic distance is of the future works.

TABLE III
GRADIENT OF THE LIGAMENT DISPLACEMENTS

Number	Roll		Pitch		Yaw	
	+	−	+	−	+	−
#0	+	−	−	+	+	+
#1	+	−	+	−	+	+
#2	−	+	+	−	+	+
#3	−	+	−	+	+	+
#4	+	−	−	−	−	+
#5	+	−	−	−	−	+
#6	−	+	−	−	+	−
#7	−	+	−	−	+	−

V. EXPERIMENTS

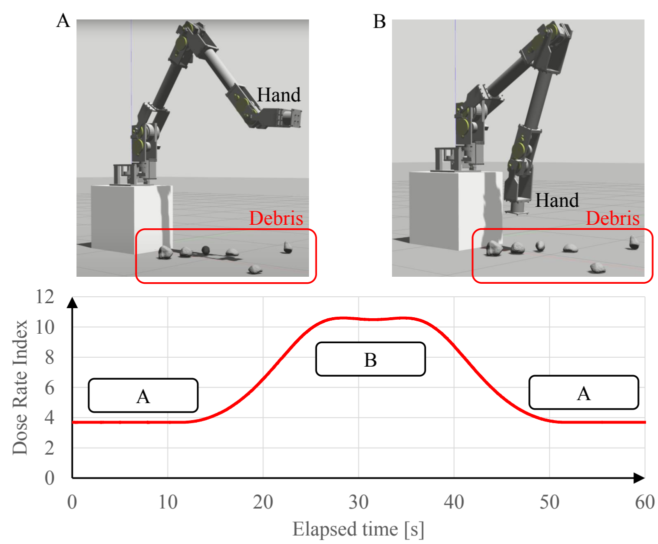

Fig. 12. Simulation utilizing the debris 3D models. The graph shows the radiation dose rate index on the robot's end effector link.

The physical simulation with the debris models is done (Fig. 12). We assumed that each debris model was a radiation source. The dose rate at the hand link can be computed by adding the reciprocal distance from the hand link to each debris. The integration to a nuclear computational framework such as Geant4 would enable the calculation of the shielding effect. Simulation of the radiation source has been investigated for radiation mapping by mobile robots intensively [20]. Calculating the effect of the robot manipulator's structure is also beneficial since the robot manipulator continues the picking task near the debris.

In Fig. 13, the validation experiment of underwater motion for the three-fingered gripper is shown. The gripper performed the open-close motion without any failure. Further research includes enhancing the finger structure's grasping force and surface friction.

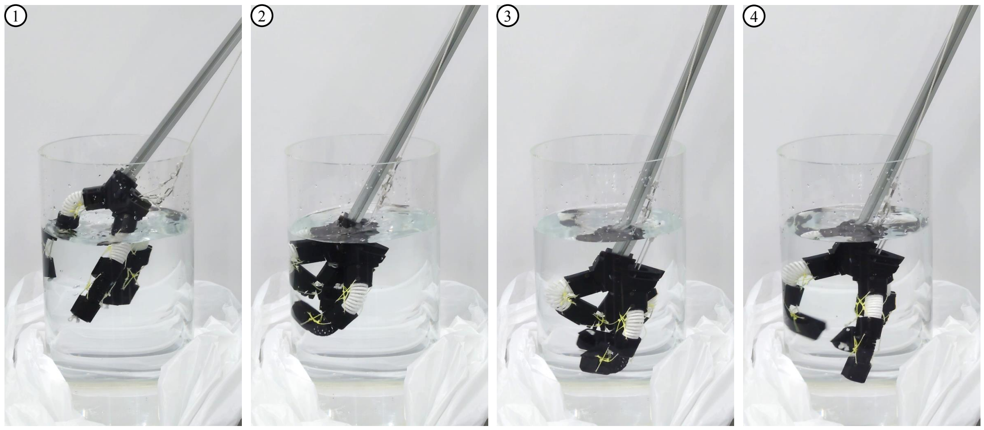

Fig. 13. Sequential photo of the underwater three-fingered gripper's motion. The tank diameter was 250 [mm], and the height was 400 [mm]. The robot gripper was immersed in the water and released from the water by the human operation. The gripper performed open and close motions without failure underwater. The gripper motion command used the same program as the two-gripper's motion.

VI. Conclusions

This paper presents the concept of fuel debris simulant as the target object dataset. The robot gripper requires characteristics such as waterproof, radiation robustness, and shock resistance. Debris simulants contribute to the design evaluation of the decommissioning robot grippers. The simulants can be generated utilizing the 3D modeling software. The 3D models can be realized with casting techniques. Future tasks include system integration with a multi-degree-of-freedom robot, debris grasping tests in a simulated environment, and verification of radiation resistance of the electrical system.

Acknowledgment

This work was supported by JAEA Nuclear Energy S&T and Human Resource Development Project Grant Number JPJA21P21476297 and JPJA24H24020026.

References

[1] Yasuyoshi Yokokohji. The use of robots to respond to nuclear accidents: Applying the lessons of the past to the fukushima daiichi nuclear power station. *Annual Review of Control, Robotics, and Autonomous Systems*, 4(1):681–710, 2021.

[2] Berk Calli, Arjun Singh, James Bruce, Aaron Walsman, Kurt Konolige, Siddhartha Srinivasa, Pieter Abbeel, and Aaron M Dollar. Yale-cmu-berkeley dataset for robotic manipulation research. *The International Journal of Robotics Research*, 36(3):261–268, 2017.

[3] Chaitanya Mitash, Fan Wang, Shiyang Lu, Vikedo Terhuja, Tyler Garaas, Felipe Polido, and Manikantan Nambi. Armbench: An object-centric benchmark dataset for robotic manipulation. In *ICRA 2023*, 2023.

[4] Huy Ha, Shubham Agrawal, and Shuran Song. Fit2Form: 3D generative model for robot gripper form design. In *Conference on Robotic Learning (CoRL)*, 2020.

[5] Zhongkui Wang, Shinichi Hirai, and Sadao Kawamura. Challenges and opportunities in robotic food handling: A review. *Frontiers in Robotics and AI*, 8, 2022.

[6] Kai Junge, Catarina Pires, and Josie Hughes. Lab2field transfer of a robotic raspberry harvester enabled by a soft sensorized physical twin. *Communications Engineering*, 2(1):40, 2023.

[7] Yuji Nagae Anton Pshenichnikov and Masaki Kurata. Comparison of the observed fukushima dai-ichi unit 2 debris with simulated debris from the clads-made-01 control blade degradation test. *Journal of Nuclear Science and Technology*, 58(4):416–425, 2021.

[8] Tadahiro Washiya, Hideki Ogino, Naoya Kaji, Yasuaki Miyamoto, and Shohei Kawaho. Properties of fuel debris. In *Proceedings of autumn session of Atomic Energy Society of JAPAN (in Japanese)*, 2005.

[9] TEPCO Holdings. Analysis of samples obtained at fukushima daiichi nuclear power station, 2022. `https://www.meti.go.jp/earthquake/nuclear/decommissioning/committee/osensuitaisakuteam/2022/04/3-3-6.pdf` (in Japanese).

[10] TEPCO Holdings. Fukushima daiichi nuclear power station unit 2: Results of the internal investigation of the reactor containment vessel, 2019. `https://www.meti.go.jp/earthquake/nuclear/decommissioning/committee/osensuitaisakuteam/2019/02/3-3-3.pdf` (in Japanese).

[11] Jay Versluis. Rock generator for blender. `https://github.com/versluis/Rock-Generator`, 2018.

[12] Christophe Journeau, Damien Roulet, Emmanuel Porcheron, Pascal Piluso, and Christophe Chagnot. Fukushima daiichi fuel debris simulant materials for the development ofăcutting and collection technologies. *Journal of Nuclear Science and Technology*, 55(9):985–995, 2018.

[13] Bernd Grambow, Ayako Nitta, Atsuhiro Shibata, Yoshikazu Koma, Satoshi Utsunomiya, Ryu Takami, Kazuki Fueda, Toshihiko Ohnuki, Christophe Jegou, Hugo Laffolley, and Christophe Journeau. Ten years after the NPP accident at Fukushima : review on fuel debris behavior in contact with water. *Journal of Nuclear Science and Technology*, 59(1):1–24, 2022.

[14] Blender Online Community. *Blender - a 3D modelling and rendering package*. Blender Foundation, Stichting Blender Foundation, Amsterdam, 2018.

[15] Shogo Makino, Kento Kawaharazuka, Ayaka Fujii, Masaya Kawamura, Tasuku Makabe, Moritaka Onitsuka, Yuki Asano, Kei Okada, Koji Kawasaki, and Masayuki Inaba. Five-fingered hand with wide range of thumb using combination of machined springs and variable stiffness joints. In *2018 IEEE/RSJ International Conference on Intelligent Robots and Systems (IROS)*, pages 4562–4567, 2018.

[16] Toshinori Hirose, Shingo Kitagawa, Shun Hasegawa, Yohei Kakiuchi, Kei Okada, and Masayuki Inaba. Waterproof soft robot hand with variable stiffness wire-driven finger mechanism using low melting point alloy for contact pressure distribution and concentration. In *2022 IEEE 5th International Conference on Soft Robotics (RoboSoft)*, pages 109–116, 2022.

[17] Gen Endo, Atsushi Horigome, and Atsushi Takata. Super dragon: A 10-m-long-coupled tendon-driven articulated manipulator. *IEEE Robotics and Automation Letters*, 4(2):934–941, 2019.

[18] Paolo Guardiani, Daniele Ludovico, Alessandro Pistone, Haider Abidi, Isiah Zaplana, Jinoh Lee, Darwin G. Caldwell, and Carlo Canali. Design and Analysis of a Fully Actuated Cable-Driven Joint for Hyper-Redundant Robots With Optimal Cable Routing. *Journal of Mechanisms and Robotics*, 14(2), 09 2021. 021006.

[19] Robert J Webster III and Bryan A Jones. Design and kinematic modeling of constant curvature continuum robots: A review. *The International Journal of Robotics Research*, 29(13):1661–1683, 2010.

[20] Thomas Wright, Andrew West, Mauro Licata, Nick Hawes, and Barry Lennox. Simulating ionising radiation in gazebo for robotic nuclear inspection challenges. *Robotics*, 10(3), 2021.